



Sulfur vacancies engineered self-supported Co_3S_4 nanoflowers as an efficient bifunctional catalyst for electrochemical water splitting

Qing Wang, Hui Xu, Xingyue Qian, Guangyu He^{*}, Haiqun Chen^{*}

Key Laboratory of Advanced Catalytic Materials and Technology, Advanced Catalysis and Green Manufacturing Collaborative Innovation Center, Changzhou University, Changzhou, Jiangsu 213164, China

ARTICLE INFO

Keywords:

Bifunctional electrocatalyst
Anion vacancy
Self-supported electrode
 Co_3S_4
Overall water splitting

ABSTRACT

Optimizing electron distribution and expediting electron transfer efficiency are two of the major strategies for developing non-noble difunctional catalysts in the overall water splitting (OWS). Defect engineering is an emerging technology in catalysis field, and introducing vacancy defects into the crystal structure can promote the electrocatalytic water splitting performance. Hence, the 3D spinel-structured Co_3O_4 or Co_3S_4 nanoflowers with anion vacancy are synthesized on nickel foam ($\text{V}_\text{o}-\text{Co}_3\text{O}_4@\text{NF}$, $\text{V}_\text{s}-\text{Co}_3\text{S}_4@\text{NF}$) and compared as electrodes for both oxygen evolution reaction (OER) and hydrogen evolution reaction (HER). Notably, $\text{V}_\text{s}-\text{Co}_3\text{S}_4@\text{NF}$ requires merely overpotential of 245 mV to reach $100 \text{ mA}\cdot\text{cm}^{-2}$ for OER, 45 mV to reach $10 \text{ mA}\cdot\text{cm}^{-2}$ for HER, which exhibit an excellent catalytic activity in alkaline electrolyte. In addition, using $\text{V}_\text{s}-\text{Co}_3\text{S}_4@\text{NF}$ as bifunctional catalyst to drive OWS, the current density of $20 \text{ mA}\cdot\text{cm}^{-2}$ is reached with a cell voltage of only 1.53 V, along with good stability for successive 200 h test.

1. Introduction

Solving the growth of energy demand and serious environmental problems, the high-efficiency and environmental-friendly new energy technologies have been widely studied [1–3]. Electrochemical water splitting is one of the representative of high-purity hydrogen production technology, which is divided into two-integral half-reaction processes: OER and HER [4,5]. To date, Ru/IrO_2 are identified as the activity-optimal catalysts for OER, while Pt/C is recognize as the most-efficient HER catalyst, but the expensiveness and scarcity of noble metal-based catalysts limit their commercial applications [6,7]. Therefore, it is essential to explore economical and durable electrocatalysts to accelerate the commercial application of OWS.

With the development of various novel synthesis strategies, characterization techniques and theoretical calculations, as an environment-friendly, abundant and low-cost catalytic material, spinel has been considered to be the most promising electrocatalyst [8–10]. Among them, oxy-spinel as an important spinel material, has been widely studied in the field of electrocatalysis because of its electrochemical features and open framework [11,12]. Although remarkable progress has been obtained, the electrocatalytic properties of most reported oxy-spinel is unsatisfactory, and the performance are not better than

that of commercial noble metal catalysts [13,14]. Accordingly, it is urgent to develop highly active spinel-based electrocatalysts. In recent years, studies have proved that thio-spinel has better electrical conductivity, mechanical properties, thermal stability and higher electrochemical activity than its corresponding oxy-spinel [15–18]. Besides, since sulfide has smaller bandgap and higher electronegativity than oxide, it can offer conspicuous electron transport effect than oxide, which is identified as one of the alternatives to noble metal catalysts [19–21].

In addition, a series of strategies also have been developed to promote the electrolysis of water processes, such as morphology engineering [22,23], defect engineering [24,25], and heterostructure engineering [26,27]. Therein, defect engineering, an important and highly efficient modification way for regulating the performances of metal centers, which can be used to reinforce the catalytic activity [28, 29]. Specifically, the electrons have been redistributed by the introduction of vacancies, which is beneficial to adjust the surface binding energy and electronic structure, enhancing the electrocatalytic activity. Furthermore, vacancies can reduce the coordination number of adjacent atoms to form new active center, improving the electrocatalytic performance in multi-step reactions, such as OER [30,31]. So far, the mechanism of oxygen anion vacancy enhancing the catalytic

^{*} Corresponding authors.

E-mail addresses: hegy@cczu.edu.cn (G. He), chenhq@cczu.edu.cn (H. Chen).

<https://doi.org/10.1016/j.apcatb.2022.122104>

Received 11 August 2022; Received in revised form 3 October 2022; Accepted 23 October 2022

Available online 27 October 2022

0926-3373/© 2022 Elsevier B.V. All rights reserved.

performance of oxy-spinel has been widely studied [32]. Moreover, a variety of strategies have been reported to successfully synthesize oxygen-defective spinel, such as reducing agent reduction [13], thermal annealing [33], and plasma etching [34]. In sharp contrast, the mechanism of thio-spinel with sulfur anion vacancy is rarely reported. One possible reason is that the higher formation energy of sulfur anion vacancies than that of oxygen anion vacancy [20]. Therefore, there are few reports on the introduction of sulfur anion defects to thio-spinel and an investigation of the structure-function relationship in the overall water splitting.

Unfortunately, the powder catalysts are usually attached to the glassy carbon electrode to fabricate the working electrode by binders in practical applications. And that, because many binders are polymer materials with poor conductivity, which hinders the effective contact surface area between the active sites of the catalyst and the electrolyte, thereby reducing the conductivity of the working electrode [35,36]. On the other hand, even with the use of binders, the adhesion of the catalysts on the glassy carbon electrode is still poor, and it cannot withstand the mechanical stresses caused by the oxygen evolution in the long-term recycle measurements, resulting in poor stability of the electrode [36, 37]. Therefore, self-growing the catalyst on the conductive substrates directly, such as nickel foam (NF), will endow the electrocatalyst with preferable adhesion to the substrate, thus improving the electron transport and mechanical stability of the electrodes [38]. Moreover, self-supported electrodes have been acted as working electrode to participate in the reaction, which not only reduces the cost, but also simplifies the operation process [39]. More importantly, it can avoid the dilemma of poor electrocatalyst conductivity and plugging of active center caused by using the binders [40].

Inspired by above points, we then determine to apply the vacancy engineering to the self-supported catalysts to design new bifunctional electrocatalysts to improve the electrocatalytic performance and durability of the OWS. Herein, we concentrate on introducing anion vacancy into cobalt-based thio-spinel structure for electrocatalytic water splitting (Scheme 1). Firstly, Co precursor grown on the NF by hydrothermal synthesis (Co-P@NF). Then, the Co_3S_4 @NF was obtained through sulphuration step. Finally, by utilizing the methods of NaBH_4 etching, the sulfur vacancy (V_s) was successfully introduced into Co_3S_4 ($\text{V}_\text{s}\text{-Co}_3\text{S}_4$ @NF). For comparison, Co_3O_4 @NF was synthesized by calcining Co-P@NF in air, and the $\text{V}_\text{o}\text{-Co}_3\text{O}_4$ @NF was obtained by the above NaBH_4 etching. In addition, the corresponding micromorphology and

structure of the electrocatalyst obtained in each step have also been fully characterized. The introduction of anion vacancy can efficiently change the electron structure around the reactive sites, promotes the adsorption of catalytic reaction intermediates, thus facilitates the OER/HER activity. As expected, the $\text{V}_\text{s}\text{-Co}_3\text{S}_4$ @NF shows outstanding electrocatalytic performance and excellent durability for both the OER (the overpotential at 100 mA cm^{-2} , denoted as η_{100} , is 245 mV) and HER ($\eta_{10} = 45 \text{ mV}$), as well as OWS (the cell only requires 1.53 V to reach 20 mA cm^{-2}).

2. Experimental section

2.1. Materials

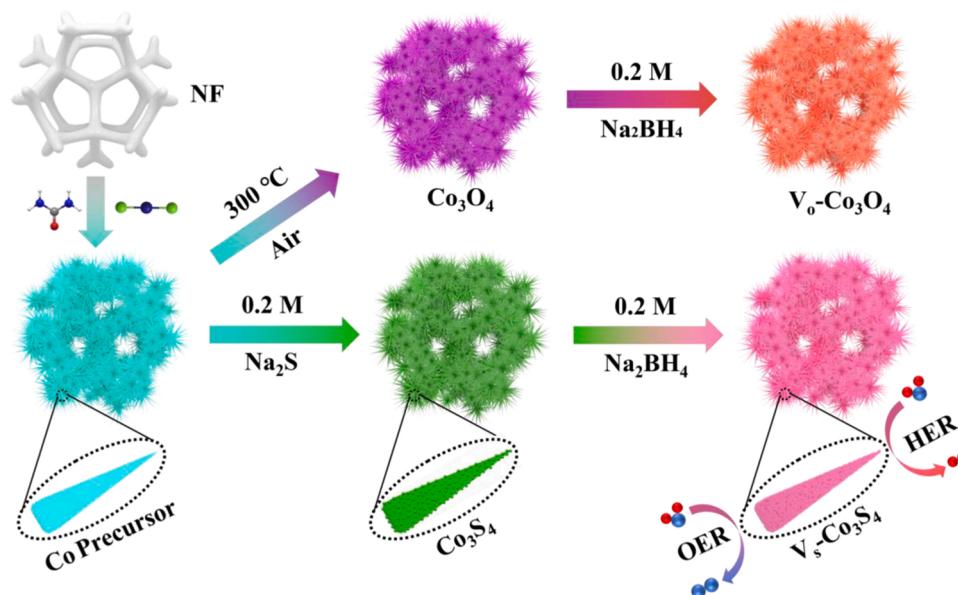
$\text{CoCl}_2 \cdot 6 \text{ H}_2\text{O}$ (AR), $\text{CO}(\text{NH}_2)_2$ (AR), NH_4F (AR), Na_2S (AR), NaBH_4 (AR), KOH (AR), HCl (AR), $\text{CH}_3\text{CH}_2\text{OH}$ (AR), and CH_3COCH_3 (AR) were obtained from Sinopharm Chemical Reagent Co., Ltd. Commercial Nickel Foam (NF) was achieved from Guangdong Canrd New Energy Technology Co., Ltd. Deionized (DI) water was obtained to prepare all aqueous solutions.

2.2. Fabrication of pristine cobalt precursor nanoflowers on NF

Firstly, NF was ultrasonically cleaned in CH_3COCH_3 , HCl , and DI water for 30 min to dispose surface impurities. The cobalt precursor (Co-P) nanoflowers was grown on NF (Co-P@NF) through a simple hydrothermal process. In detail, 1 mmol of $\text{CoCl}_2 \cdot 6 \text{ H}_2\text{O}$ was dissolved into 30 mL DI water and stirred for 10 min, then 2 mmol of $\text{CO}(\text{NH}_2)_2$ was added to the above solution to form a homogeneous aqueous solution under stirred for 10 min. Next, 3 mmol of NH_4F was added to the mixture and stirred for another 10 min to obtain a transparent solution. Subsequently, a piece of NF ($1 \times 2 \text{ cm}^2$) was put into a 50 mL Teflon-lined stainless steel autoclave, the above solution was also poured into autoclave, and heated at 120°C for 15 h. Finally, the obtained product was taken out, and washed for further use, and denoted as Co-P@NF.

2.3. Fabrication of Co_3O_4 and $\text{V}_\text{o}\text{-Co}_3\text{O}_4$ on NF

The as-synthesized Co-P@NF was annealed at 300°C for 2 h with a heating rate of 5°C min^{-1} in air atmosphere, and denoted as Co_3O_4 @NF. The Co_3O_4 with oxygen vacancies on NF was obtained by



Scheme 1. Schematic diagram of the synthesis process of $\text{V}_\text{o}\text{-Co}_3\text{O}_4$ @NF and $\text{V}_\text{s}\text{-Co}_3\text{S}_4$ @NF.

soaking the above $\text{Co}_3\text{O}_4@\text{NF}$ in 50 mL of 0.2 M NaBH_4 solution at 25 °C for 10 min, then washed for further use, and denoted as $\text{V}_o\text{-Co}_3\text{O}_4@\text{NF}$.

2.4. Fabrication of Co_3S_4 and $\text{V}_s\text{-Co}_3\text{S}_4$ on NF

The as-synthesized $\text{Co-P}@\text{NF}$ was immersed in 30 mL 0.2 M Na_2S solution and hydrothermally treated at 160 °C for 15 h. Then, the obtained product was taken out, washed for further use, and denoted as $\text{Co}_3\text{S}_4@\text{NF}$. The Co_3S_4 with sulfur vacancies on NF was obtained by soaking the above $\text{Co}_3\text{S}_4@\text{NF}$ in 50 mL of 0.2 M NaBH_4 solution at 25 °C for 10 min, then washed for further use, and denoted as $\text{V}_s\text{-Co}_3\text{S}_4@\text{NF}$.

2.5. Electrochemical measurement

The OER, HER, and OWS test were performed on a Chenhua electrochemical workstation (CHI 760E). The electrocatalytic performance were studied in a three-electrode device, consisted of a self-support catalyst, a Hg/HgO electrode, and a graphite rod, serving as working electrode (WE), reference electrode (RE), and counter electrode (CE), respectively. The electrochemical measurements were executed in 1 M KOH. Linear sweep voltammetry (LSV) curves were obtained with the scan rate of $5 \text{ mV}\cdot\text{s}^{-1}$. The chronoamperometric measurements for OER and HER were carried out at 100 and $-100 \text{ mA}\cdot\text{cm}^{-2}$ for 100 h. Cyclic voltammetry (CV) curves were carried out at various scan rates to estimate electrochemical active surface area (ECSA) of the catalysts. The electrochemical impedance spectroscopy (EIS) was tested at the overpotential for OER and HER within frequency window ranging from 100 kHz to 0.01 Hz. Long-term chronoamperometric tests were performed at corresponding potential to deliver a current density of $100 \text{ mA}\cdot\text{cm}^{-2}$. All measured potentials were calibrated with respect to

the reversible hydrogen electrode (RHE), and based on the formula: $E_{\text{RHE}} = E_{\text{Hg}/\text{HgO}} + 0.0592 \times \text{pH} + 0.098$. The OWS performance was assessed using a CHI 760E electrochemical workstation in a two-electrode system, and self-support catalysts as both the anode and cathode, respectively.

2.6. Computational details

DFT calculations were performed to analyze the structural features of the catalyst, using the Cambridge sequential total energy package (CASTEP) code provided by Materials Studio (MS). In details, the value of cut-off energy was set as 500 eV for Plane Wave basis function. The Monkhorst-Pack k-point meshes with the size of $5 \times 5 \times 5$ was obtained to sample bulk Brillouin zone of the electronic properties. The convergence criteria for energy were set with the value of $1.0 \times 10^{-5} \text{ eV}$ unit cell and ground-state atomic geometries were optimized by relaxing the force less than $0.02 \text{ eV}\cdot\text{\AA}^{-1}$.

3. Results and discussion

3.1. Microstructure characterization

The microstructure details of the Co_3O_4 and Co_3S_4 before and after the NaBH_4 treatment were first executed to investigate by the scanning electron microscopy (SEM). As shown in Fig. 1a, the SEM image of $\text{Co}_3\text{O}_4@\text{NF}$ reflects that it is assembled by the stochastic distributed nanoneedles to form nanoflowers and grown on the NF uniformly and densely. Besides, the transmission electron microscopy (TEM) image of $\text{Co}_3\text{O}_4@\text{NF}$ further demonstrated the nanoneedle-like structure, in which numerous uniform nanoneedles were distributed uniformly on

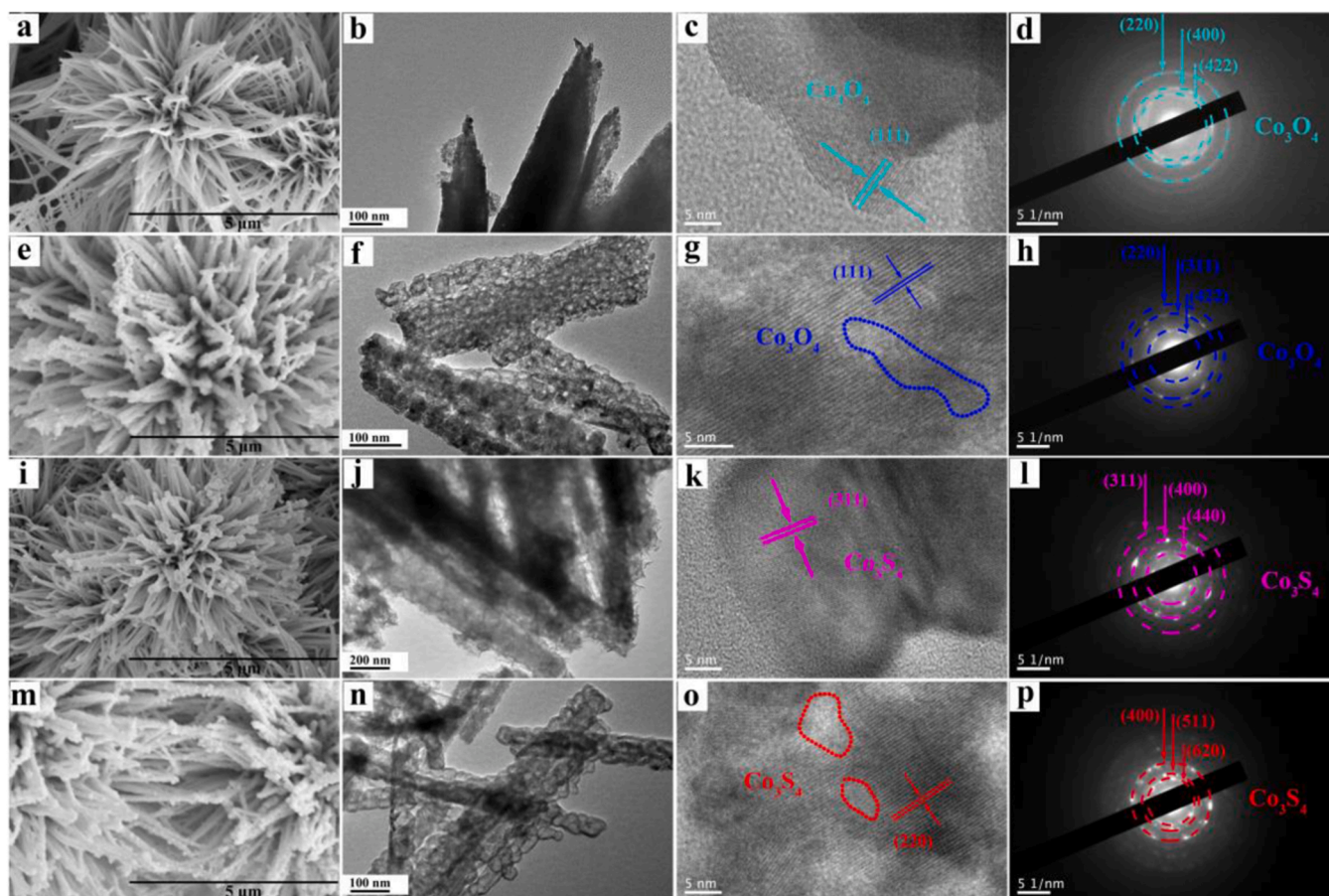


Fig. 1. SEM, TEM, and HR-TEM images, SAED patterns of (a-d) $\text{Co}_3\text{O}_4@\text{NF}$, (e-h) $\text{V}_o\text{-Co}_3\text{O}_4@\text{NF}$, (i-l) $\text{Co}_3\text{S}_4@\text{NF}$, and (m-p) $\text{V}_s\text{-Co}_3\text{S}_4@\text{NF}$.

the surface of NF (Fig. 1b). High-resolution TEM (HR-TEM) image of the $\text{Co}_3\text{O}_4@\text{NF}$ displays that the interplanar spacing of 0.465 nm is consistent with the spacing of the (111) plane of the spinel Co_3O_4 crystal (Fig. 1c) [41]. The selected area electron diffraction (SAED) pattern of the $\text{Co}_3\text{O}_4@\text{NF}$ also exhibits clear diffraction rings of the (220), (400) and (422) plane, revealing the existence of spinel Co_3O_4 phase (Fig. 1d) [42]. For $\text{V}_0\text{-Co}_3\text{O}_4@\text{NF}$, the nanoflowers morphology was completely retained after NaBH_4 etching, but the original smooth nanoneedle surface becomes rough (Fig. 1e) [13]. It can be obviously observed in the TEM image (Fig. 1f), the wrinkled nanoneedles actually become porous structures and are composed of closely connected nanoparticles. The HR-TEM image (Fig. 1g) also presents lattice fringes corresponding to the (111) lattice plane of Co_3O_4 , while the disorganized lattice fringe (labeled by blue dashed) reveals the existence of defects [32]. Besides, the SAED pattern (Fig. 1h) manifests diffraction spots of (220), (311), and (422), which are matched well with the Co_3O_4 crystal [33]. The above results verify the presence of the oxygen vacancy, which proves the formation of $\text{V}_0\text{-Co}_3\text{O}_4@\text{NF}$ structure.

As clearly denoted in Fig. 1i, the $\text{Co}_3\text{S}_4@\text{NF}$ maintains the nano-flower morphology without any evident changes, but the needle surface of $\text{Co}_3\text{S}_4@\text{NF}$ becomes fluffy (Fig. 1j) when compared with $\text{Co}_3\text{O}_4@\text{NF}$. Fig. 1k exhibits that the interplanar spacing of 0.285 nm of $\text{Co}_3\text{S}_4@\text{NF}$ is consistent with the spacing of the (311) plane of the spinel Co_3S_4 crystal. The SAED pattern (Fig. 1l) displays diffraction rings attributing to (311), (400), and (440) planes of Co_3S_4 [18]. In differentiating with the morphology of $\text{V}_0\text{-Co}_3\text{O}_4@\text{NF}$, the porous structure of $\text{V}_s\text{-Co}_3\text{S}_4@\text{NF}$ surface becomes large and sparse after NaBH_4 etching (Fig. 1m, n) [43], and the larger voids accelerate electrolyte ingress throughout the entire structure. Many dislocations are observed in $\text{V}_s\text{-Co}_3\text{S}_4@\text{NF}$ nanoflowers, as labeled by the red circle circles in Fig. 1o, which suggests the existence of defect-rich structure. The SEAD image of $\text{V}_s\text{-Co}_3\text{S}_4@\text{NF}$ in Fig. 1p exhibits the diffraction of the (400), (511), and (620) crystal planes of the Co_3S_4 , which is in line with XRD results [44]. Furthermore, all NF substrates were connected to each other to form a continuous three-dimensional (3D) network, and the stable connection between the NF and the catalyst promotes mass transfer and charge transport

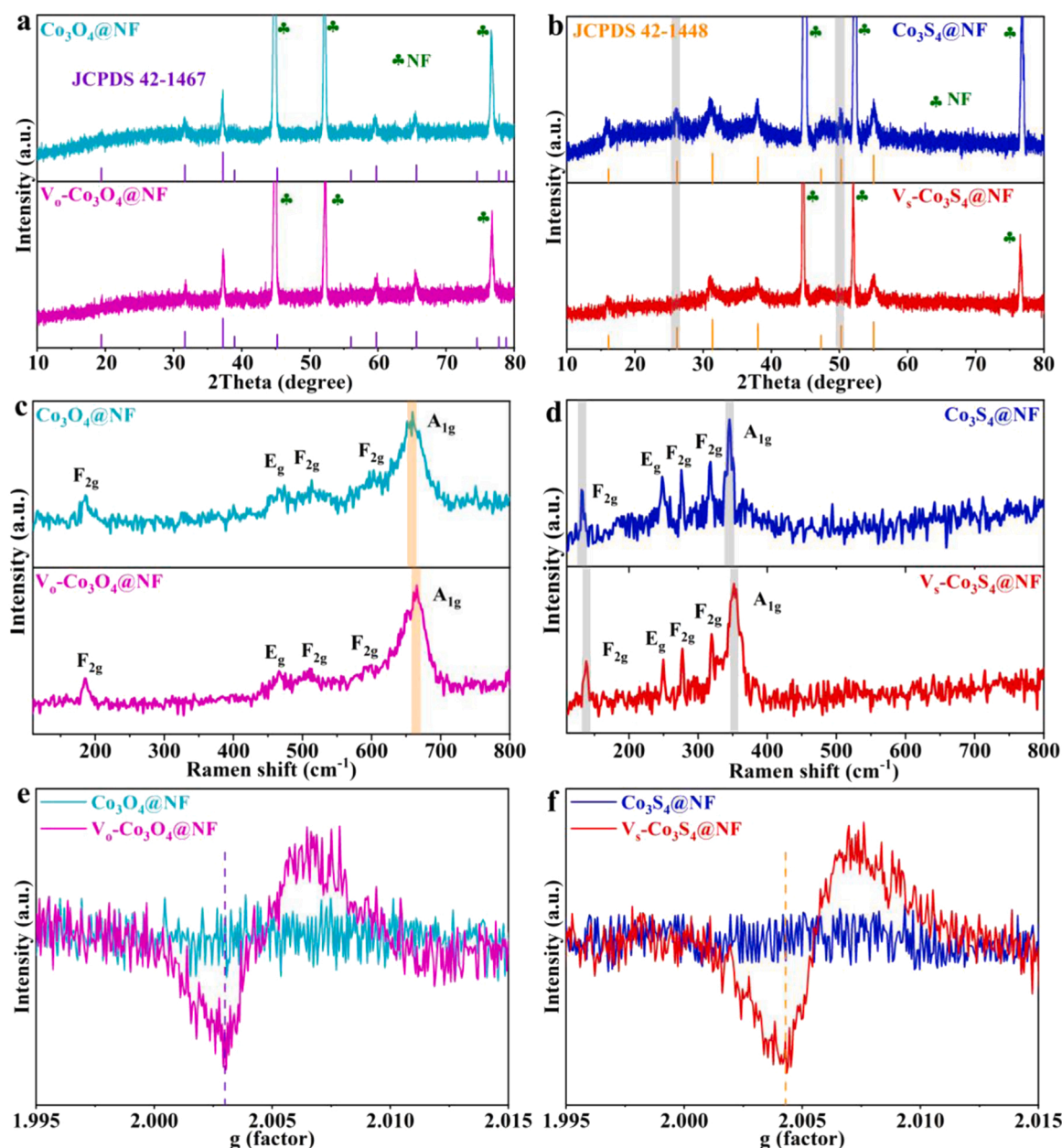


Fig. 2. (a, b) XRD patterns, (c, d) Raman spectrum, and (e, f) EPR spectra of $\text{Co}_3\text{O}_4@\text{NF}$, $\text{V}_0\text{-Co}_3\text{O}_4@\text{NF}$, $\text{Co}_3\text{S}_4@\text{NF}$, and $\text{V}_s\text{-Co}_3\text{S}_4@\text{NF}$.

processes in the catalytic reactions (Fig. S1).

3.2. Structure characterization

The X-ray diffraction (XRD) was carried out to characterize the crystalline structures of the catalysts, and results were showed in Fig. 2a,

b. Firstly, three strong diffraction peaks belonging to NF (JCPDS 04-0850) were observed at $2\theta = 44.9^\circ$, 52.1° , and 76.5° for all catalysts. As denoted in Fig. 2a, except the diffraction peak of NF, all the other peaks at 2θ of 19.01° , 31.25° , 36.89° , 59.36° , 65.24° are originated from the (111), (220), (311), (511), and (440) reflections, corresponding to the standard spinel Co_3O_4 crystal (JCPDS 42-1467), which is in line with

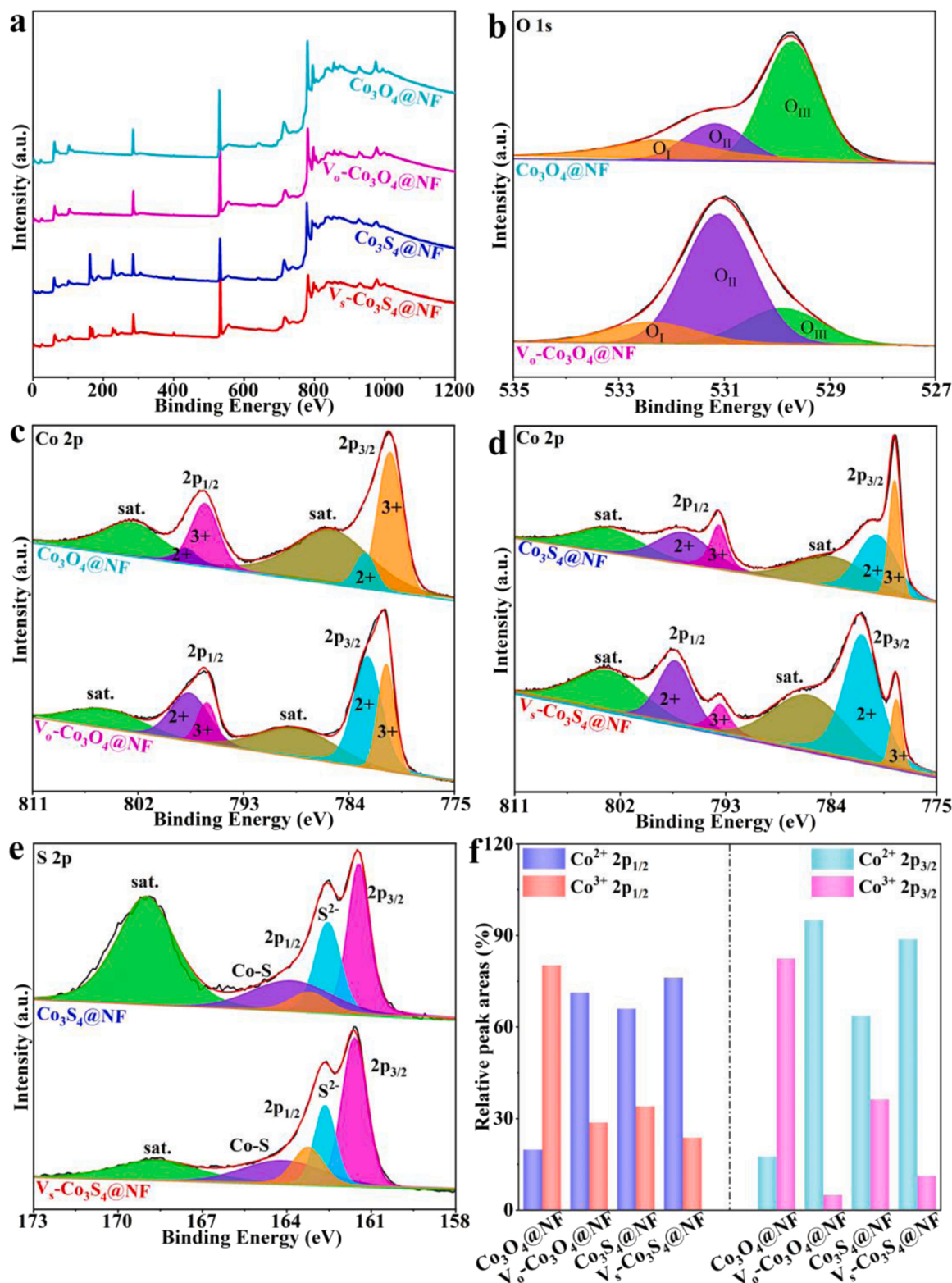


Fig. 3. (a) XPS survey spectrum of $\text{Co}_3\text{O}_4@\text{NF}$, $\text{Co}_3\text{S}_4@\text{NF}$, $\text{V}_6\text{-Co}_3\text{O}_4@\text{NF}$, and $\text{V}_5\text{-Co}_3\text{S}_4@\text{NF}$. High-resolution XPS of (b) O 1s, (c-d) Co 2p, and (e) S 2p. (f) The relative peak areas of Co^{2+} and Co^{3+} in the catalysts.

the characterization results of HR-TEM and SAED [45]. After vulcanization, the Co precursor was completely transformed into Co_3S_4 ($\text{Co}_3\text{S}_4/\text{NF}$) as evidenced by new diffraction peaks at 2θ of 16.11° , 26.71° , 31.42° , 38.05° , 47.29° , 50.23° , and 55.01° , corresponding to the (111), (220), (311), (400), (422), (511), and (440) planes of standard spinel Co_3S_4 crystal (JCPDS 42-1448), respectively (Fig. 2b) [46]. In comparison with $\text{Co}_3\text{S}_4/\text{NF}$, the diffraction peaks of $\text{V}_s\text{-Co}_3\text{S}_4/\text{NF}$ at 26.67° and 50.23° are disappeared, which can be classified as the existence of sulfur vacancies, revealing more anion defects of $\text{V}_s\text{-Co}_3\text{S}_4/\text{NF}$. The Raman spectrum of all catalysts were exhibited in Fig. 2c, the spectra of $\text{Co}_3\text{O}_4/\text{NF}$ and $\text{V}_o\text{-Co}_3\text{O}_4/\text{NF}$ display the same vibration peaks including F_2g , E_g , and A_1g , which is consistent well with the characteristic peaks of Co_3O_4 . Compared to the $\text{Co}_3\text{O}_4/\text{NF}$, the main peak of $\text{V}_o\text{-Co}_3\text{O}_4/\text{NF}$ at 660 cm^{-1} shows a distinct blue-shift and broadening of the A_1g peak after NaBH_4 reduction (yellow dash area), which might be caused by the formation of oxygen vacancies [47].

Furthermore, five characteristic peaks of F_2g (133, 275, and 316 cm^{-1}), E_g (250 cm^{-1}), A_1g (347 cm^{-1}) belonging to the phonon modes of Co_3S_4 have been seen in both $\text{Co}_3\text{S}_4/\text{NF}$ and $\text{V}_s\text{-Co}_3\text{S}_4/\text{NF}$ (Fig. 2d). The Raman peaks of $\text{V}_s\text{-Co}_3\text{S}_4/\text{NF}$ displays a tendency to move to a lower direction (grey dash area), which may due to the expansion of cell caused by the generation of sulfur vacancies [43,48]. The electron paramagnetic resonance (EPR) technology was employed to confirm the inherent defects in the $\text{V}_o\text{-Co}_3\text{O}_4/\text{NF}$ and $\text{V}_s\text{-Co}_3\text{S}_4/\text{NF}$. As depicted in Fig. 2e, owing to the existence of oxygen vacancies in the lattice, a wide signal peak generates at $g = 2.003$ [49]. Meanwhile, and the signal appears at $g = 2.004$ (Fig. 2f) is associated with the unpaired electron capture after the formation of sulfur vacancies in the lattice [31]. On the one hand, compared with $\text{V}_o\text{-Co}_3\text{O}_4/\text{NF}$, the EPR signal peak of $\text{V}_s\text{-Co}_3\text{S}_4/\text{NF}$ was apparently more intensified and widened, revealing the existence of more sulfur vacancies in $\text{V}_s\text{-Co}_3\text{S}_4/\text{NF}$ [50]. On the other hand, more sulfur vacancies can enhance free charge carrier, expose more active sites, and promote electrolyte ions mobility, which is favorable to electrochemical activity.

It is generally believed that the formation of anion vacancies is attributed to the reduction of Co^{3+} to Co^{2+} for Co-based electrocatalysts. Thus, the relative content of Co^{2+} is another significant factor to characterize vacancies formation [51]. Therefore, the X-ray photoelectron spectroscopy (XPS) was performed to characterize the chemical valence state of Co element, and infer the valence change of the Co_3O_4 and Co_3S_4 before and after etching. Firstly, the XPS full-survey spectra illustrates that the existence of Co, O elements in the $\text{Co}_3\text{O}_4/\text{NF}$ and $\text{V}_o\text{-Co}_3\text{O}_4/\text{NF}$ [33], while Co, S elements in the $\text{Co}_3\text{S}_4/\text{NF}$ and $\text{V}_s\text{-Co}_3\text{S}_4/\text{NF}$ (Fig. 3a) [52]. The high-resolution O 1s spectra of $\text{Co}_3\text{O}_4/\text{NF}$ and $\text{V}_o\text{-Co}_3\text{O}_4/\text{NF}$ are shown in Fig. 3b, the three peaks are individually caused by Co-O bond (O_I), O vacancies (O_II) and O-O(H) (O_III). In contrast to $\text{Co}_3\text{O}_4/\text{NF}$, the higher peak near at 531.2 eV of $\text{V}_o\text{-Co}_3\text{O}_4/\text{NF}$, indicating that the formation of abundant hypoxic co-ordination defect sites [53], and the percentages of O_I , O_II , and O_III are summarized in Table S3. This conclusion is corresponding to the EPR result, in which the presence of oxygen vacancies in $\text{V}_o\text{-Co}_3\text{O}_4/\text{NF}$. The high-resolution Co 2p spectra of $\text{Co}_3\text{O}_4/\text{NF}$ were exhibited in Fig. 3c and f, the peaks located at 797.9 and 782.6 eV are corresponded to Co^{2+} , while the other two characteristic peaks situated at 796.3 and 780.5 eV are indexed to Co^{3+} . Apparently, the Co 2p spectrum of $\text{V}_o\text{-Co}_3\text{O}_4/\text{NF}$ had also been divided into two characteristic peaks of Co^{2+} and Co^{3+} [32]. Whereas, a higher percentage of the ratio of $\text{Co}^{2+}/\text{Co}^{3+}$ (Table S1) were observed in $\text{V}_o\text{-Co}_3\text{O}_4/\text{NF}$ by comparison with unetched $\text{Co}_3\text{O}_4/\text{NF}$, which is attributed to more Co species with low coordination number at the edge sites triggered after NaBH_4 etching. The above results significantly imply the existence of oxygen vacancies in $\text{V}_o\text{-Co}_3\text{O}_4/\text{NF}$.

As clearly manifested in Fig. 3d, the peaks at near 778.6 and 780.1 eV , 793.6 and 796.6 eV have been attributed to the binding energies of Co $2\text{p}_{3/2}$ and Co $2\text{p}_{1/2}$ of $\text{Co}_3\text{S}_4/\text{NF}$ and $\text{V}_s\text{-Co}_3\text{S}_4/\text{NF}$, respectively. According to XPS-peak differentiation-imitating analysis

(Table S2), it is clear that the ratio of $\text{Co}^{2+}/\text{Co}^{3+}$ in $\text{V}_s\text{-Co}_3\text{S}_4/\text{NF}$ is 2.91 , which is higher than other catalysts, demonstrating that partial Co^{3+} were reduced to Co^{2+} , and more Co^{2+} ions were generated after NaBH_4 etching, which indicating that the formation of sulfur vacancies in $\text{V}_s\text{-Co}_3\text{S}_4/\text{NF}$ (Fig. 3f) [54]. Furthermore, five well-resolved peaks were detected in the S 2p XPS spectrum, as shown in Fig. 3e. The peak near at 169.0 eV is attributed to the satellite (sat.) peak, and 164.0 eV is the characteristic peaks of Co-S compounds, while the characteristic peak appears at 162.6 eV is ascribed to the existence of S^{2-} in a low coordination state on the surface of catalysts. In addition, the doublets near at 163.3 and 161.5 eV are ascribed to the S $2\text{p}_{1/2}$ and S $2\text{p}_{3/2}$, respectively. Interestingly, the relative peak area ratio of S $2\text{p}_{1/2}$ was 0.06 for $\text{Co}_3\text{S}_4/\text{NF}$, and this ratio increased to 0.14 for $\text{V}_s\text{-Co}_3\text{S}_4/\text{NF}$ (Table S4) [52]. This result reveals the existence of sulfur vacancies in the $\text{V}_s\text{-Co}_3\text{S}_4/\text{NF}$, which could improve the Volmer step among the catalytic process and kinetics of H_2O adsorption, thereby reduces the Tafel slope of OER and HER processes.

3.3. OER electrocatalysis measurement

The three-electrode electrochemical device was carried out to test the catalytic performance of all electrocatalysts to OER in 1.0 M KOH solution. As references, NF and RuO_2/NF were also analyzed under the same test conditions. Fig. 4a exhibits the LSV curves of all electrocatalysts, the designed $\text{V}_s\text{-Co}_3\text{S}_4/\text{NF}$ displays extraordinary OER performance with an overpotential of merely 245 mV to offer $100\text{ mA}\cdot\text{cm}^{-2}$, which is better than $\text{Co}_3\text{S}_4/\text{NF}$ (332 mV), $\text{V}_o\text{-Co}_3\text{O}_4/\text{NF}$ (262 mV), $\text{Co}_3\text{O}_4/\text{NF}$ (393 mV), and RuO_2/NF (470 mV). Moreover, the $\text{V}_s\text{-Co}_3\text{S}_4/\text{NF}$ requires merely 470 mV overpotential to achieve a high current density of $300\text{ mA}\cdot\text{cm}^{-2}$, implying the tremendous potential toward industrial applications. In addition, it can be seen from Fig. 4b that the $\text{V}_s\text{-Co}_3\text{S}_4/\text{NF}$ has the highest current density at both high and low potentials, further demonstrating the excellent OER activity. Their intrinsic OER kinetics were also evaluated by Tafel plot, the results are illustrated in Fig. 4c [55]. The Tafel slope of $\text{V}_s\text{-Co}_3\text{S}_4/\text{NF}$ is merely $60\text{ mV}\cdot\text{dec}^{-1}$, which is much lower than that of $\text{Co}_3\text{S}_4/\text{NF}$ ($122\text{ mV}\cdot\text{dec}^{-1}$), $\text{V}_o\text{-Co}_3\text{O}_4/\text{NF}$ ($116\text{ mV}\cdot\text{dec}^{-1}$), and $\text{Co}_3\text{O}_4/\text{NF}$ ($128\text{ mV}\cdot\text{dec}^{-1}$), demonstrating that $\text{V}_s\text{-Co}_3\text{S}_4/\text{NF}$ has relatively rapid electron transition and remarkable OER catalytic reaction kinetics. In order to further study the intrinsic catalytic activity of catalysts, the turnover frequency (TOF) is calculated in Table S5. The TOF of $\text{V}_s\text{-Co}_3\text{S}_4/\text{NF}$ is $0.023\text{ mol O}_2\text{ s}^{-1}$, which is much higher than that of $\text{V}_o\text{-Co}_3\text{O}_4/\text{NF}$ ($0.016\text{ mol O}_2\text{ s}^{-1}$), indicating that the intrinsic catalytic activity of $\text{V}_s\text{-Co}_3\text{S}_4/\text{NF}$ is higher than $\text{V}_o\text{-Co}_3\text{O}_4/\text{NF}$. Furthermore, the EIS is another essential parameter for estimating reaction kinetics. Fig. 4d displays that the charge transfer resistance (R_ct) value of $\text{V}_s\text{-Co}_3\text{S}_4/\text{NF}$ was $0.7\text{ }\Omega$, which is also much lower than that of $\text{Co}_3\text{S}_4/\text{NF}$ ($2.46\text{ }\Omega$), $\text{V}_o\text{-Co}_3\text{O}_4/\text{NF}$ ($1.43\text{ }\Omega$), and $\text{Co}_3\text{O}_4/\text{NF}$ ($7.16\text{ }\Omega$), suggesting the fastest charge transfer efficiency and OER kinetics [56].

Aiming to further explore different electrochemical activity of all catalysts, the double-layer capacitance (C_dl) was tested from the CV curves to estimate the ECSA [57]. As shown in Fig. 4e, the C_dl value of catalysts were calculated according to their CV curves (Fig. S2). The C_dl value of $\text{V}_s\text{-Co}_3\text{S}_4/\text{NF}$ is $52\text{ mF}\cdot\text{cm}^{-2}$, apparently higher than those of $\text{Co}_3\text{S}_4/\text{NF}$ ($20\text{ mF}\cdot\text{cm}^{-2}$), $\text{V}_o\text{-Co}_3\text{O}_4/\text{NF}$ ($34\text{ mF}\cdot\text{cm}^{-2}$), and $\text{Co}_3\text{O}_4/\text{NF}$ ($5\text{ mF}\cdot\text{cm}^{-2}$), revealing increased ECSA and more available active sites of $\text{V}_s\text{-Co}_3\text{S}_4/\text{NF}$. In general, the multi-current curve of the catalyst is obtained by changing the different current densities to assist in judging the stability of the catalyst. Therefore, the multi-current curve of $\text{V}_s\text{-Co}_3\text{S}_4/\text{NF}$ was achieved by altering the current density from 50 to $250\text{ mA}\cdot\text{cm}^{-2}$ at a rate of $50\text{ mA}\cdot\text{cm}^{-2}$ per 1000 s . It can be seen from Fig. 4f, the potential stabilized immediately at 1.39 V for $50\text{ mA}\cdot\text{cm}^{-2}$, no matter increases or decreases of the current density, the obtained potential remains virtually unchanged within 1000 s . Similar results were observed under other current density, indicating that $\text{V}_s\text{-Co}_3\text{S}_4/\text{NF}$ electrode had the excellent mass transfer, electronic

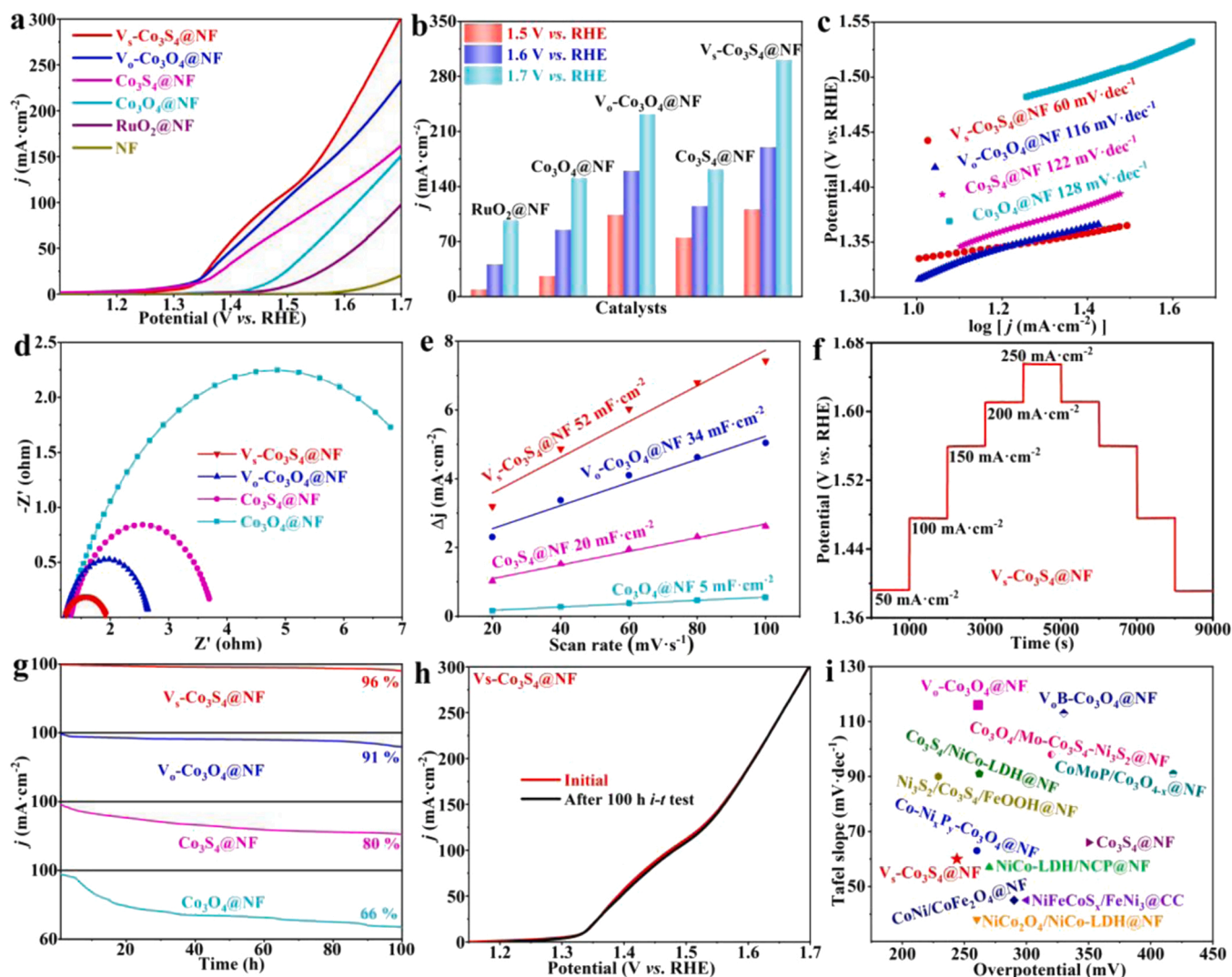


Fig. 4. (a) LSV curves, (b) Required current densities at different potential vs RHE, (c) Tafel slopes, (d) EIS plots, and (e) C_{dl} of different electrocatalysts. (f) The multi-current process of $V_5\text{-Co}_3\text{S}_4\text{@NF}$ (50–250 $\text{mA}\cdot\text{cm}^{-2}$). (g) the i - t curves of all electrocatalysts. (h) LSV curves of $V_5\text{-Co}_3\text{S}_4\text{@NF}$ before and after 100 h OER i - t test. (i) Comparisons of OER performances in kinetics and overpotential at 100 $\text{mA}\cdot\text{cm}^{-2}$ on $V_5\text{-Co}_3\text{S}_4\text{@NF}$, $V_0\text{-Co}_3\text{O}_4\text{@NF}$, and Co-based OER catalysts reported previously.

conductivity, and mechanical stability. Compared with other catalysts, $V_5\text{-Co}_3\text{S}_4\text{@NF}$ exhibits outstanding long-term stability as proof by its unalterable chrono-potentiometric curves after 100 h at a current density of 100 $\text{mA}\cdot\text{cm}^{-2}$, as depicted in Fig. 4g. Furthermore, Fig. 4h displays that the LSV curve of $V_5\text{-Co}_3\text{S}_4\text{@NF}$ was basically unchanged after 100 chronoamperometric (i - t) test, which further confirmed its excellent cycle stability. More importantly, compared with most Co-based OER catalysts reported formerly, $V_5\text{-Co}_3\text{S}_4\text{@NF}$ still shows excellent OER performance and kinetics, as shown in Fig. 4i and Table S6.

3.4. HER electrocatalysis measurement

The electrocatalytic activity of all catalysts toward HER was assessed by polarization curves in 1.0 M KOH solution. Fig. 5a manifests that the polarization curve of the $V_5\text{-Co}_3\text{S}_4\text{@NF}$ is the most outstanding, and it shows the current densities of 100 $\text{mA}\cdot\text{cm}^{-2}$ can be achieved only require the overpotential of 275 mV, which is smaller than the $V_0\text{-Co}_3\text{O}_4\text{@NF}$ (397 mV), $\text{Co}_3\text{S}_4\text{@NF}$ (339 mV), and $\text{Co}_3\text{O}_4\text{@NF}$ (386 mV), indicating that $V_5\text{-Co}_3\text{S}_4\text{@NF}$ can enhance the electrocatalytic activity significantly. In order to compare the performance of catalysts clearly, the overpotentials at the current densities of 100, 150, and 200 $\text{mA}\cdot\text{cm}^{-2}$ were shown in Fig. 5b. The required overpotentials of $V_5\text{-Co}_3\text{S}_4\text{@NF}$

were 275, 299, and 318 mV to achieve the current densities of 100, 150, and 200 $\text{mA}\cdot\text{cm}^{-2}$, which are much smaller than those of $\text{Co}_3\text{S}_4\text{@NF}$ (339, 364, and 378 mV), $V_0\text{-Co}_3\text{O}_4\text{@NF}$ (297, 318, and 334 mV), and $\text{Co}_3\text{O}_4\text{@NF}$ (386, 422, and 450 mV), respectively. Except the low overpotential, the Tafel plot is also a major indicator to evaluate the electrocatalytic reaction rate. The smaller Tafel slope demonstrates the faster the reaction rate. It can be seen from Fig. 5c, the Tafel slopes of $\text{Co}_3\text{O}_4\text{@NF}$, $V_0\text{-Co}_3\text{O}_4\text{@NF}$, $\text{Co}_3\text{S}_4\text{@NF}$, and $V_5\text{-Co}_3\text{S}_4\text{@NF}$ were 215, 120, 77, and 66 $\text{mV}\cdot\text{dec}^{-1}$, respectively, and Pt/C@NF also reached 84 $\text{mV}\cdot\text{dec}^{-1}$, reflecting that the $V_5\text{-Co}_3\text{S}_4\text{@NF}$ has superior HER kinetics. In addition, EIS test was performed to further understand the charge transfer kinetics. Similarly, the smaller EIS illustrates the faster charge transfer and the better electrocatalytic activity. As shown in Fig. 5d, according to Nyquist plots, the R_{ct} of $V_5\text{-Co}_3\text{S}_4\text{@NF}$ is the smallest, indicating that the value of EIS is the smallest, which is beneficial to promote HER catalytic activity of $V_5\text{-Co}_3\text{S}_4\text{@NF}$.

The ECSA of all electrocatalysts were achieved by C_{dl} in non-Faradaic potential region (Fig. S3) to further estimate the electrocatalytic performance improvement. Because the C_{dl} is directly proportional to the ECSA, thus the larger the C_{dl} indicates the larger the ECSA. As clearly depicted in Fig. 5e, the C_{dl} value of $V_5\text{-Co}_3\text{S}_4\text{@NF}$, $V_0\text{-Co}_3\text{O}_4\text{@NF}$, $\text{Co}_3\text{S}_4\text{@NF}$, and $\text{Co}_3\text{O}_4\text{@NF}$ were 155, 23, 127, and 18 $\text{mF}\cdot\text{cm}^{-2}$,

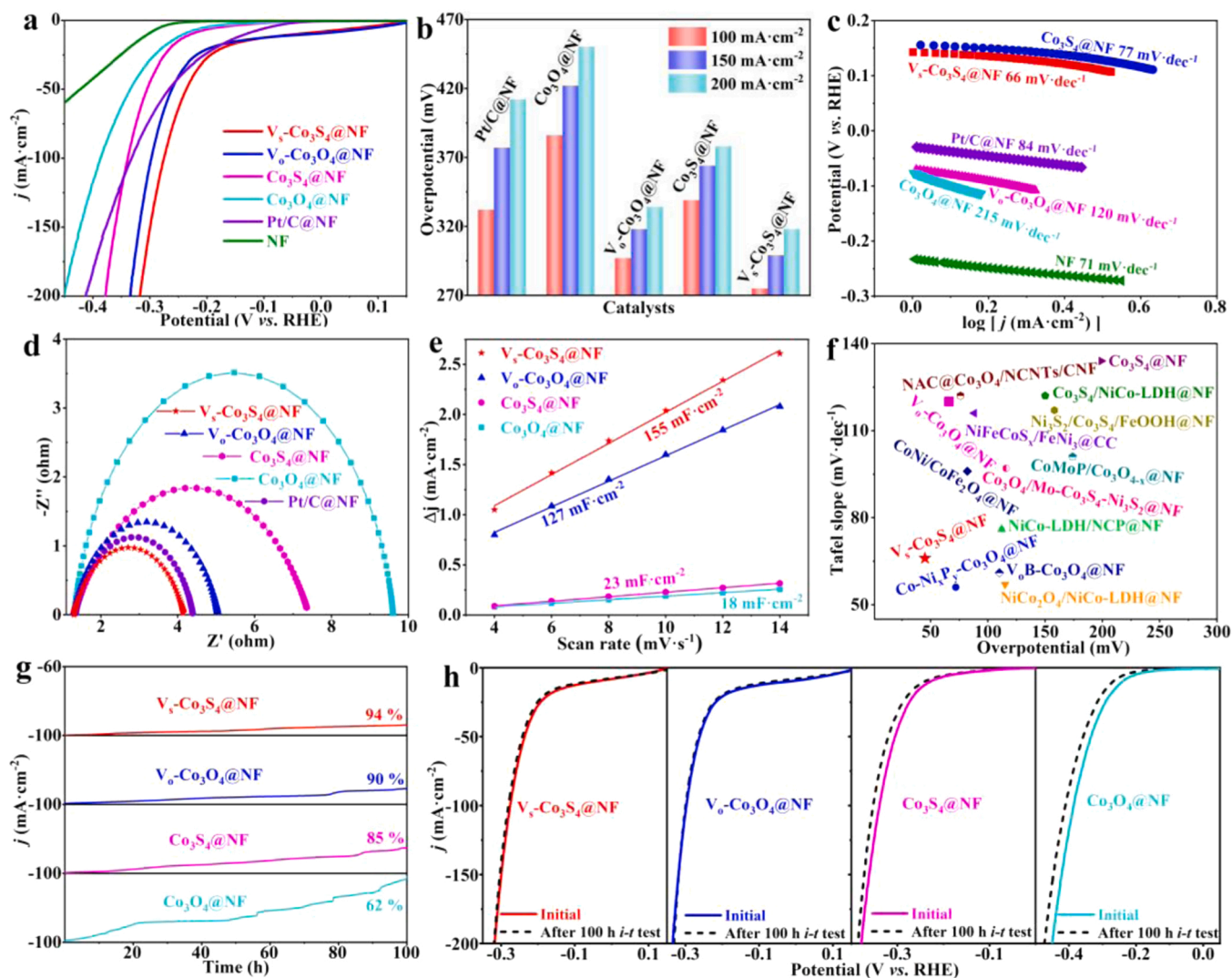


Fig. 5. (a) LSV curves, (b) Bar graph showing the required overpotential needed to achieve a current density of 100, 150, and 200 $\text{mA}\cdot\text{cm}^{-2}$, (c) Tafel slopes, (d) Nyquist plots, and (e) C_{dl} of different electrocatalysts. (f) Comparisons of HER performances in kinetics and overpotential at 100 $\text{mA}\cdot\text{cm}^{-2}$ on $\text{V}_s\text{-Co}_3\text{S}_4\text{@NF}$, $\text{V}_o\text{-Co}_3\text{O}_4\text{@NF}$, and Co-based HER catalysts reported previously. (g) the i - t curves of all electrocatalysts. (h) LSV curves of $\text{V}_s\text{-Co}_3\text{S}_4\text{@NF}$ before and after 100 h i - t test for HER.

respectively. Therefore, $\text{V}_s\text{-Co}_3\text{S}_4\text{@NF}$ has the largest ECSA, indicating that the introduction of sulfur vacancies exposes the most active sites in the electrolyte, thereby promoting HER catalytic activity. In terms of the low overpotential and Tafel slope, the $\text{V}_s\text{-Co}_3\text{S}_4\text{@NF}$ is superior to reported most HER electrocatalysts, as depicted in Fig. 5f and Table S7. Besides, the cyclic performance is an important factor to estimate high-activity electrocatalysts. The i - t test of catalysts were performed at a constant overpotential for 100 h, as denoted in Fig. 5g. It must also be mentioned that the current density of $\text{V}_s\text{-Co}_3\text{S}_4\text{@NF}$ decreased by only 6%, which is significantly superior to those of other electrocatalysts, indicating the outstanding stability of $\text{V}_s\text{-Co}_3\text{S}_4\text{@NF}$ for the HER. Additionally, Fig. 5h depicts that after 100 h i - t test, the polarization curve of $\text{V}_s\text{-Co}_3\text{S}_4\text{@NF}$ showed no notable decay compared with the initial one, while other catalysts have certain decay, and further demonstrating the outstanding stability of the $\text{V}_s\text{-Co}_3\text{S}_4\text{@NF}$. These data indicate that it is difficult for catalysts with oxygen vacancies or without vacancies to maximize HER performance, while the catalysts with the sulfur vacancies have excellent HER activity, which is similar to the findings of OER conclusions.

3.5. OWS performance measurement

The bifunctional catalytic performance of the $\text{V}_s\text{-Co}_3\text{S}_4\text{@NF}$ in OWS could be better assessed by combining OER and HER activity. As denoted in Fig. 6a, $\text{V}_s\text{-Co}_3\text{S}_4\text{@NF}$ shows a much lower potential difference of 1.63 V ($\Delta E = E_{j=50(\text{OER})} - E_{j=50(\text{HER})}$) than that of $\text{Co}_3\text{S}_4\text{@NF}$ (1.74 V), $\text{Co}_3\text{O}_4\text{@NF}$ (1.88 V), $\text{V}_o\text{-Co}_3\text{O}_4\text{@NF}$ (1.67 V), demonstrating the outstanding bifunctional catalytic activity towards OWS for $\text{V}_s\text{-Co}_3\text{S}_4\text{@NF}$. Considering the distinguished both OER and HER performance of $\text{V}_s\text{-Co}_3\text{S}_4\text{@NF}$, a simple two-electrode device was constructed using $\text{V}_s\text{-Co}_3\text{S}_4\text{@NF}$ as both anode and cathode for actual application (Fig. 6b). For comparison, the $\text{Co}_3\text{O}_4\text{@NF} \parallel \text{Co}_3\text{O}_4\text{@NF}$, $\text{Co}_3\text{S}_4\text{@NF} \parallel \text{Co}_3\text{S}_4\text{@NF}$, $\text{V}_o\text{-Co}_3\text{O}_4\text{@NF} \parallel \text{V}_o\text{-Co}_3\text{O}_4\text{@NF}$, and $\text{RuO}_2 \parallel \text{Pt/C}$ electrodes are shown in Fig. 6c. It is proved that $\text{V}_s\text{-Co}_3\text{S}_4\text{@NF} \parallel \text{V}_s\text{-Co}_3\text{S}_4\text{@NF}$ electrode requires only a cell voltage of 1.45 V to achieve a current density of 10 $\text{mA}\cdot\text{cm}^{-2}$, which outperform the any one of $\text{Co}_3\text{S}_4\text{@NF} \parallel \text{Co}_3\text{S}_4\text{@NF}$ (1.53 V), $\text{Co}_3\text{O}_4\text{@NF} \parallel \text{Co}_3\text{O}_4\text{@NF}$ (1.67 V), $\text{V}_o\text{-Co}_3\text{O}_4\text{@NF} \parallel \text{V}_o\text{-Co}_3\text{O}_4\text{@NF}$ (1.49 V), and $\text{RuO}_2 \parallel \text{Pt/C}$ electrodes (1.68 V). Fig. 6f shows the photograph of the fabricated $\text{V}_s\text{-Co}_3\text{S}_4\text{@NF}$ electrode configuration for water splitting. It is worthwhile mentioning that plenty of gas bubbles were generated on the surface of $\text{V}_s\text{-Co}_3\text{S}_4\text{@NF} \parallel \text{V}_s\text{-Co}_3\text{S}_4\text{@NF}$ electrode.

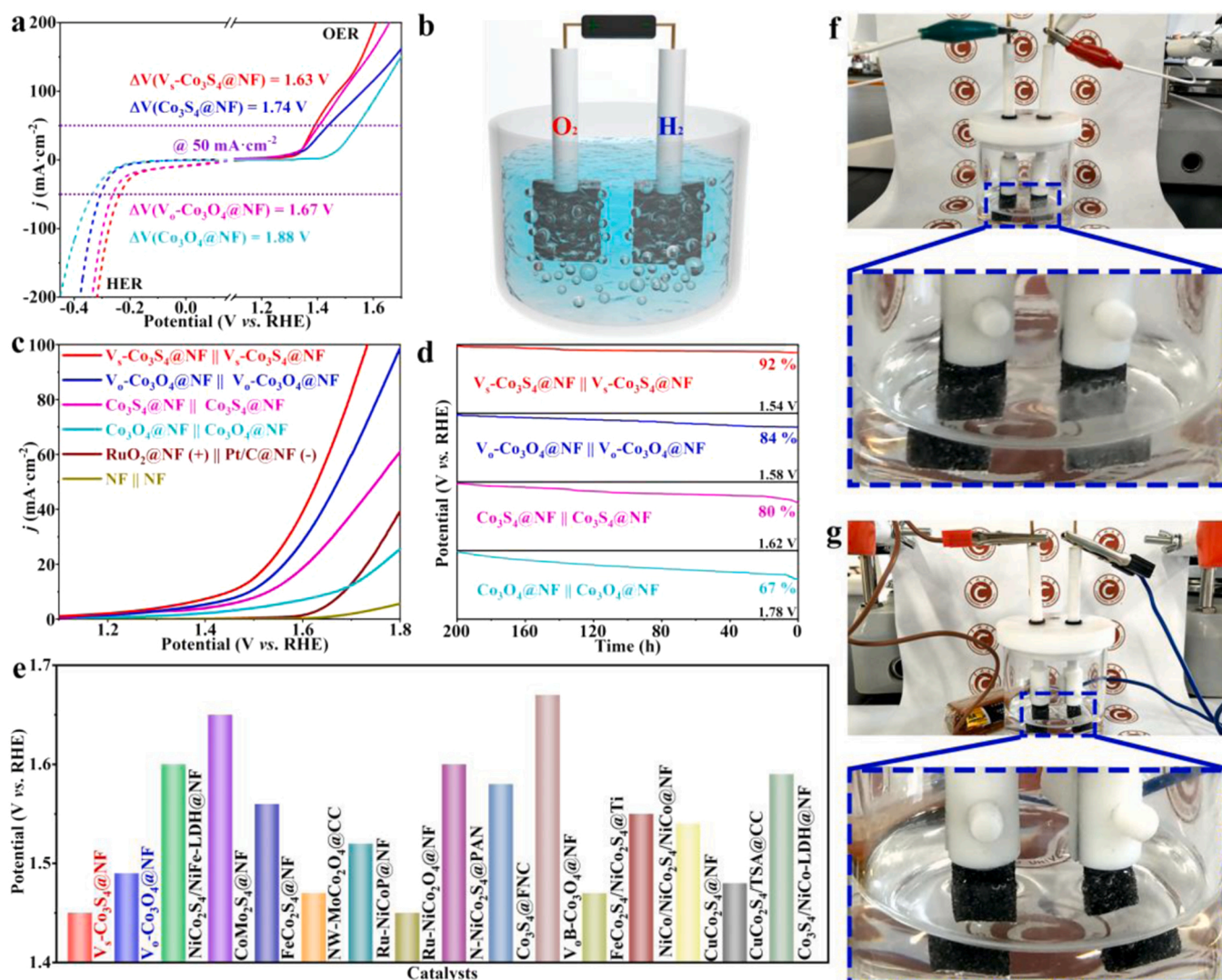


Fig. 6. (a) Bifunctional activities for different catalysts. (b) Schematic illustration of overall water electrolysis cell. (c) The LSV of $V_s\text{-Co}_3\text{S}_4\text{@NF} || V_s\text{-Co}_3\text{S}_4\text{@NF}$, $V_o\text{-Co}_3\text{O}_4\text{@NF} || V_o\text{-Co}_3\text{O}_4\text{@NF}$, $\text{Co}_3\text{S}_4\text{@NF} || \text{Co}_3\text{S}_4\text{@NF}$, $\text{Co}_3\text{O}_4\text{@NF} || \text{Co}_3\text{O}_4\text{@NF}$, $\text{RuO}_2\text{@NF} || \text{Pt/C@NF}$, and $\text{NF} || \text{NF}$ toward OWS. (d) The chrono-potentiometric curve of $V_s\text{-Co}_3\text{S}_4\text{@NF} || V_s\text{-Co}_3\text{S}_4\text{@NF}$, $V_o\text{-Co}_3\text{O}_4\text{@NF} || V_o\text{-Co}_3\text{O}_4\text{@NF}$, $\text{Co}_3\text{S}_4\text{@NF} || \text{Co}_3\text{S}_4\text{@NF}$, and $\text{Co}_3\text{O}_4\text{@NF} || \text{Co}_3\text{O}_4\text{@NF}$ at $20\text{ mA}\cdot\text{cm}^{-2}$. (e) Comparison of $V_s\text{-Co}_3\text{S}_4\text{@NF}$, $V_o\text{-Co}_3\text{O}_4\text{@NF}$ with other bifunctional electrocatalysts. (f) Photograph of the fabricated two-electrode configuration for water splitting. (g) Photograph of the fabricated water electrolyzer using a single 1.5 V AA battery-powered for OWS.

In addition, as showed in Fig. 6d, the cycling stability of $V_s\text{-Co}_3\text{S}_4\text{@NF} || V_s\text{-Co}_3\text{S}_4\text{@NF}$ electrode was also estimated, which can work for over 200 h at the current density of $20\text{ mA}\cdot\text{cm}^{-2}$, and the driving voltage decreased by only about 8%, which is better than that of the $V_o\text{-Co}_3\text{O}_4\text{@NF}$ (16%), $\text{Co}_3\text{S}_4\text{@NF}$ (24%), and $\text{Co}_3\text{O}_4\text{@NF}$ (33%), verifying its outstanding cycling stability. Furthermore, it is worth noting that the $V_s\text{-Co}_3\text{S}_4\text{@NF}$ electrolyzer is superior to others Co-based electrolyzers (Fig. 6e, Table S8). To our knowledge, there are little attention about the electrocatalysis driving the alkaline OWS by a single 1.5 V AA battery up to now. Therefore, the $V_s\text{-Co}_3\text{S}_4\text{@NF}$ act as both the anode and cathode were assembled into a cell, powered by a single self-assembly 1.5 V AA battery device. Interestingly, it is worth noting that plenty of O₂ gas bubbles were generated from the anode surface and a number of H₂ bubbles are generated from the cathode surface (Fig. 6g), which is sufficient to indicate that $V_s\text{-Co}_3\text{S}_4\text{@NF}$ has potential commercial application in water splitting.

3.6. Mechanistic Investigation

To investigate the advantages of the $V_s\text{-Co}_3\text{S}_4\text{@NF}$ for enhancing the

OER and HER activity, first principles density functional theory (DFT) calculation was carried out to analyze the crystal structural characteristics of the $\text{Co}_3\text{S}_4\text{@NF}$ and $V_s\text{-Co}_3\text{S}_4\text{@NF}$, using the CASTE code provided by MS. Band structure and total density of state (TDOS) were calculated to illustrate the changes in electronic structure after introduction of sulfur vacancy. Firstly, Fig. S4 is the atomic structure models of the $\text{Co}_3\text{S}_4\text{@NF}$ and $V_s\text{-Co}_3\text{S}_4\text{@NF}$. In contrast to $\text{Co}_3\text{S}_4\text{@NF}$, the impurity bands near the Fermi level of $V_s\text{-Co}_3\text{S}_4\text{@NF}$ are dense and stable, which may improve the conductivity of electron from the valence band (VB) to the conduction band (CB), demonstrating that the introduction of sulfur vacancies effectively improves the carrier concentration and the electrical conductivity of $\text{Co}_3\text{S}_4\text{@NF}$, as manifested in Fig. S5. In addition, the TDOS of $\text{Co}_3\text{S}_4\text{@NF}$ and $V_s\text{-Co}_3\text{S}_4\text{@NF}$ were shown in Fig. S6, the formation of sulfur vacancies promoted the increase of TDOS for $V_s\text{-Co}_3\text{S}_4\text{@NF}$ (green rectangle in Fig. S6), resulting in the decrease of OOH* binding strength on the surface of the $V_s\text{-Co}_3\text{S}_4\text{@NF}$, reducing the reaction energy barrier and improving the electrocatalytic performance, which is consistent with the experimental results [58].

It is reported that Co_3S_4 will be oxidized to metal hydroxides/oxyhydroxides on the surface of Co_3S_4 in the OER procedure, and plays a

precatalytic role as a true catalytic active site. In order to investigate the changes of surface structure and chemical valence state, the TEM, XRD, EPR, and XPS characterizations of the $V_s\text{-Co}_3\text{S}_4\text{@NF}$ were carried out after 100 h OER and HER stability test. As shown in Fig. S7–S8, the porous structure of $V_s\text{-Co}_3\text{S}_4\text{@NF}$ is still maintained after OER and HER test, demonstrating the superior stability. The XRD characterization of $V_s\text{-Co}_3\text{S}_4\text{@NF}$ after long-term OER process demonstrating that except Co_3S_4 crystalline phase, the new crystalline phase of $\text{Co}(\text{OH})_2$ and CoOOH can be also detected in $V_s\text{-Co}_3\text{S}_4\text{@NF}$ (Fig. S9). This phenomenon indicates that Co_3S_4 was partially transformed into $\text{Co}(\text{OH})_2$ and CoOOH after the long-term OER catalytic reaction. Notably, the EPR test shows that the peak intensity of vacancy is relatively weaker, which means that the content of sulfur vacancies is relatively reduced after OER catalysis (Fig. S11). However, it may also be attributed to the Co_3S_4 or Co_3O_4 was partially converted to highly active $\text{Co}(\text{OH})_2$ or CoOOH , so OER activity is almost unchanged. In addition, the cubic crystal structure $V_s\text{-Co}_3\text{S}_4\text{@NF}$ after HER test was almost unchanged compared with the pristine $V_s\text{-Co}_3\text{S}_4\text{@NF}$ (Fig. S10). Fig. S12 displays the full XPS spectrum of $V_s\text{-Co}_3\text{S}_4\text{@NF}$ after 100 h OER stability test. It shows the presence of Co and S elements in the catalyst. Surprisingly, it was found that the binding energies are obviously positive shifted at $\text{Co } 2p_{3/2}$ and $\text{Co } 2p_{1/2}$, indicating that low valence state of Co^{2+} was oxidized to Co^{3+} (Fig. S13a). Furthermore, the new peaks appears at 783.51 and 780.19 eV occur in the high-resolution Co 2p spectrum, corresponding to the $\text{Co}(\text{OH})_2$ and CoOOH phases, and confirming the existence of hydroxides or/and oxyhydroxides as the real active center after 100 h OER *i-t* test [52]. In addition, the intensity of the $\text{Co } 2p_{3/2}$ and $\text{Co } 2p_{1/2}$ are obviously decreased, demonstrating that S element was seriously leached after 100 h OER *i-t* test (Fig. S13b). After 100 h HER *i-t* test, the impurity peak is invisible in the full XPS survey spectra of $V_s\text{-Co}_3\text{S}_4\text{@NF}$ (Fig. S12), and the peaks in the Co 2p and S 2p spectra (Fig. S14) were basically unchanged, demonstrating that the valence state of $V_s\text{-Co}_3\text{S}_4\text{@NF}$ has only little variation, which confirms the excellent stability of $V_s\text{-Co}_3\text{S}_4\text{@NF}$ in the HER process. The above conclusions clearly demonstrate that the long-term OER test process undergo the phase transition, Co_3S_4 was converted into $\text{Co}(\text{OH})_2/\text{CoOOH}$, and actually act as the catalytic active sites, while the long-term HER don't change visibly.

4. Conclusion

In summary, sulfur vacancies-rich Co_3S_4 nanoflowers were grown on nickel foam via hydrothermal and reduction strategies ($V_s\text{-Co}_3\text{S}_4\text{@NF}$), and assembled as a superior bifunctional electrocatalysts for OWS. Owing to the creation of abundant sulfur vacancies, the $V_s\text{-Co}_3\text{S}_4$ can not only provide more electrochemically active sites, but also accelerate electron transport, which improve its electronic conductivity. In addition, the self-assembled 3D structure can keep the completeness of the catalyst microstructure and inhibit the clustering of active species in the electrolysis process, thereby enhancing the OWS catalysis performance. The $V_s\text{-Co}_3\text{S}_4\text{@NF}$ shows outstanding catalytic performance for OWS with the overpotential of only 245 mV at the current density of $100 \text{ mA}\cdot\text{cm}^{-2}$ for OER, and the overpotential of merely 46 mV at the current density of $10 \text{ mA}\cdot\text{cm}^{-2}$ for HER in 1 M KOH solution. Moreover, an electrolytic cell with $V_s\text{-Co}_3\text{S}_4\text{@NF}$ as both anode and cathode were established, which merely required the cell voltage of 1.53 V to reach $20 \text{ mA}\cdot\text{cm}^{-2}$, and can also be powered by a single self-assembly 1.5 V AA battery device, indicating that $V_s\text{-Co}_3\text{S}_4\text{@NF}$ had potential application in water splitting. The catalytic activity is comparable to that of all the catalysts reported at present. This work developed a facial and practical approach for the fabrication of sulfur vacancy catalysts, opened a new sight for effective and durable electrocatalysts, which exhibit tremendous potential for the exploration of an enhanced commercial OWS procedure.

CRediT authorship contribution statement

Qing Wang: Software, Data curation, Investigation, DFT calculations, Writing – original draft, **Hui Xu:** Investigation, Software, **Xingyue Qian:** Software, Data curation, **Guangyu He:** Supervision, Conceptualization, Writing – review & editing, **Haiqun Chen:** Supervision, Writing – review & editing, Project administration.

Declaration of Competing Interest

The authors declare that they have no known competing financial interests or personal relationships that could have appeared to influence the work reported in this paper.

Data Availability

Data will be made available on request.

Acknowledgements

The authors are grateful for the financial support from National Natural Science Foundation of China (No. 21978026, 22078028), Postgraduate Research & Practice Innovation Program of Jiangsu Province (No. KYCX22_3032), Scientific Research Foundation of Jiangsu Provincial Education Department (No. 21KJB430034), Leading Innovative Talents Introduction and Cultivation Project of Changzhou (No. CQ20210114). Prof. Yin for MS software support. Changzhou University Computer Center for computing services.

Appendix A. Supporting information

Supplementary data associated with this article can be found in the online version at doi:10.1016/j.apcatb.2022.122104.

References

- [1] N.S. Lewis, A prospective on energy and environmental science, *Energy Environ. Sci.* 12 (2019) 16–18.
- [2] E. Lebre, M. Stringer, K. Svobodova, J.R. Owen, D. Kemp, C. Cote, A. Arratia-Solar, R.K. Valenta, The social and environmental complexities of extracting energy transition metals, *Nat. Commun.* 11 (2020) 8.
- [3] H. Xu, Y. Zhao, Q. Wang, G. He, H. Chen, Supports promote single-atom catalysts toward advanced electrocatalysis, *Coord. Chem. Rev.* 451 (2022), 214261.
- [4] X. Li, J. Zhou, C. Liu, L. Xu, C. Lu, J. Yang, H. Pang, W. Hou, Encapsulation of Janus-structured Ni/Ni₂P nanoparticles within hierarchical wrinkled N-doped carbon nanofibers: Interface engineering induces high-efficiency water oxidation, *Appl. Catal. B* 298 (2021), 120578.
- [5] X. Li, C. Liu, Z. Fang, L. Xu, C. Lu, W. Hou, Ultrafast room-temperature synthesis of self-supported nife-layered double hydroxide as large-current-density oxygen evolution electrocatalyst, *Small* 18 (2022), 2104354.
- [6] L. Tian, H. Chen, X. Lu, D. Liu, W. Cheng, Y. Liu, J. Li, Z. Li, Local photothermal and photoelectric effect synergistically boost hollow $\text{CeO}_2/\text{CoS}_2$ heterostructure electrocatalytic oxygen evolution reaction, *J. Colloid Interface Sci.* 628 (2022) 663–672.
- [7] H. Xu, C. Wang, G. He, H. Chen, Y. Du, Hierarchical hollow $\text{CoWO}_4\text{-Co}(\text{OH})_2$ heterostructured nanoboxes enabling efficient water oxidation electrocatalysis, *Inorg. Chem.* 61 (2022) 14224–14232.
- [8] G.P. Wu, J. Wang, W. Ding, Y. Nie, L. Li, X.Q. Qi, S.G. Chen, Z.D. Wei, A strategy to promote the electrocatalytic activity of spinels for oxygen reduction by structure reversal, *Angew. Chem. Int. Ed.* 55 (2016) 1340–1344.
- [9] D. Wang, Y. Chen, L. Fan, T. Xiao, T. Meng, Z. Xing, X. Yang, Bulk and surface dual modification of nickel-cobalt spinel with ruthenium toward highly efficient overall water splitting, *Appl. Catal. B* 305 (2022), 121081.
- [10] X.-M. Liu, X. Cui, K. Dastafkan, H.-F. Wang, C. Tang, C. Zhao, A. Chen, C. He, M. Han, Q. Zhang, Recent advances in spinel-type electrocatalysts for bifunctional oxygen reduction and oxygen evolution reactions, *J. Energy Chem.* 53 (2021) 290–302.
- [11] J. Ge, W. Zhang, J. Tu, T. Xia, S. Chen, G. Xie, Suppressed Jahn-Teller distortion in $\text{MnCo}_2\text{O}_4/\text{Ni}_2\text{P}$ heterostructures to promote the overall water splitting, *Small* 16 (2020), 2001856.
- [12] Y. Peng, C. Huang, J. Huang, M. Feng, X. Qiu, X. Yue, S. Huang, Filling octahedral interstices by building geometrical defects to construct active sites for boosting the oxygen evolution reaction on NiFe_2O_4 , *Adv. Funct. Mater.* 32 (2022), 2201011.
- [13] H. Yuan, S. Wang, Z. Ma, M. Kundu, B. Tang, J. Li, X. Wang, Oxygen vacancies engineered self-supported B doped Co_3O_4 nanowires as an efficient multifunctional

- catalyst for electrochemical water splitting and hydrolysis of sodium borohydride, *Chem. Eng. J.* 404 (2021), 126474.
- [14] Y. Huang, S.L. Zhang, X.F. Lu, Z.P. Wu, D. Luan, X.W.D. Lou, Trimetallic spinel $\text{NiCo}_{2-x}\text{Fe}_x\text{O}_4$ nanoboxes for highly efficient electrocatalytic oxygen evolution, *Angew. Chem. Int. Ed.* 60 (2021) 11841–11846.
- [15] L. Wu, L. Sun, X. Li, Q. Zhang, Y. Zhang, J. Gu, K. Wang, Y. Zhang, CuCo_2S_4 -rGO microflowers: first-principle calculation and application in energy storage, *Small* 16 (2020), 2001468.
- [16] L. Shao, Z.-X. Liang, H. Chen, Z.-X. Song, X.-H. Deng, G. Huo, X.-M. Kang, L. Wang, X.-Z. Fu, J.-L. Luo, CuCo_2S_4 hollow nanoneedle arrays supported on Ni foam as efficient trifunctional electrocatalysts for overall water splitting and Al-air, *Batter. J. Alloy. Compd.* 845 (2020), 155392.
- [17] Y. Liang, Q. Gong, X. Sun, N. Xu, P. Gong, J. Qiao, Rational fabrication of thin-layered NiCo_2S_4 loaded graphene as bifunctional non-oxide catalyst for rechargeable zinc-air batteries, *Electrochim. Acta* 342 (2020), 136108.
- [18] A.T. Aqueel Ahmed, A.S. Ansari, H. Kim, H. Im, Ion-exchange synthesis of microporous Co_3S_4 for enhanced electrochemical energy storage, *Int. J. Energy Res.* 46 (2021) 5315–5329.
- [19] D. Wang, L. Tian, J. Huang, D. Li, J. Liu, Y. Xu, H. Ke, Q. Wei, “One for two” strategy to prepare MOF-derived NiCo_2S_4 nanorods grown on carbon cloth for high-performance asymmetric supercapacitors and efficient oxygen evolution reaction, *Electrochim. Acta* 334 (2020), 135636.
- [20] T.-F. Yi, J.-J. Pan, T.-T. Wei, Y. Li, G. Cao, NiCo_2S_4 -based nanocomposites for energy storage in supercapacitors and batteries, *Nano Today* 33 (2020), 100894.
- [21] Y. Li, J. Li, Y. Pan, Z. Xiong, G. Yao, R. Xie, B. Lai, Peroxymonosulfate activation on FeCo_2S_4 modified g- C_3N_4 (FeCo_2S_4 -CN): mechanism of singlet oxygen evolution for nonradical efficient degradation of sulfamethoxazole, *Chem. Eng. J.* 384 (2020), 123361.
- [22] S. Tang, Y. Zhou, X. Lu, Z. Chen, Z. Huang, Z. Li, L. Tian, Surface/interface engineering for fabricating hierarchical Ir doped NiMoO_4 covered by Co/Ni layered double hydroxide toward oxygen evolution reaction, *J. Alloy. Compd.* 924 (2022), 166415.
- [23] Q. Wang, H. Xu, X.Y. Qian, B.J. Huang, K. Wang, L. Jin, G.Y. He, H.Q. Chen, Successive anion/cation exchange enables the fabrication of hollow CuCo_2S_4 nanorods for advanced oxygen evolution reaction electrocatalysis, *Inorg. Chem.* 61 (2022) 3176–3185.
- [24] D. Yan, Y. Li, J. Huo, R. Chen, L. Dai, S. Wang, Defect chemistry of nonprecious-metal electrocatalysts for oxygen reactions, *Adv. Mater.* 29 (2017), 1606459.
- [25] Z. Wu, Y. Zhao, W. Jin, B. Jia, J. Wang, T. Ma, Recent Progress of vacancy engineering for electrochemical energy conversion related applications, *Adv. Funct. Mater.* 31 (2020), 2009070.
- [26] W.-Z. Chen, M. Zhang, Y. Liu, X.-M. Yao, P.-Y. Liu, Z. Liu, J. He, Y.-Q. Wang, Super-hydrophilic $\text{MgO}/\text{NiCo}_2\text{S}_4$ heterostructure for high-efficient oxygen evolution reaction in neutral electrolytes, *Appl. Catal. B* 312 (2022), 121432.
- [27] L. Tan, J. Yu, C. Wang, H. Wang, X. Liu, H. Gao, L. Xin, D. Liu, W. Hou, T. Zhan, Partial sulfidation strategy to $\text{NiFe-LDH}/\text{FeNi}_2\text{S}_4$ heterostructure enable high-performance water/seawater oxidation, *Adv. Funct. Mater.* 32 (2022), 2200951.
- [28] S. Wang, H. Wang, B. Konig, Light-induced single-electron transfer processes involving sulfur anions as catalysts, *J. Am. Chem. Soc.* 143 (2021) 15530–15537.
- [29] J. Pan, G. Zhang, Z. Guan, Q. Zhao, G. Li, J. Yang, Q. Li, Z. Zou, Anchoring Ni single atoms on sulfur-vacancy-enriched ZnIn_2S_4 nanosheets for boosting photocatalytic hydrogen evolution, *J. Energy Chem.* 58 (2021) 408–414.
- [30] H. Su, S. Song, Y. Gao, N. Li, Y. Fu, L. Ge, W. Song, J. Liu, T. Ma, In situ electronic redistribution tuning of NiCo_2S_4 nanosheets for enhanced electrocatalysis, *Adv. Funct. Mater.* 32 (2021), 2109731.
- [31] X. Gu, S. Li, W. Shao, X. Mu, Y. Yang, Y. Ge, W. Meng, G. Liu, S. Liu, S. Mu, Cation/anion dual-vacancy pair modulated atomically-thin $\text{Se}_x\text{-Co}_3\text{S}_4$ nanosheets with extremely high water oxidation performance in ultralow-concentration alkaline solutions, *Small* 18 (2022), 2108097.
- [32] J. Lv, L. Wang, R. Li, K. Zhang, D. Zhao, Y. Li, X. Li, X. Huang, G. Wang, Constructing a hetero-interface composed of oxygen vacancy-enriched Co_3O_4 and crystalline-amorphous NiFe-LDH for oxygen evolution reaction, *ACS Catal.* 11 (2021) 14338–14351.
- [33] S. Guan, L. An, S. Ashraf, L. Zhang, B. Liu, Y. Fan, B. Li, Oxygen vacancy excites Co_3O_4 nanocrystals embedded into carbon nitride for accelerated hydrogen generation, *Appl. Catal.* 269 (2020), 118775.
- [34] Z. Xiao, Y. Wang, Y.-C. Huang, Z. Wei, C.-L. Dong, J. Ma, S. Shen, Y. Li, S. Wang, Filling the oxygen vacancies in Co_3O_4 with phosphorus: an ultra-efficient electrocatalyst for overall water splitting, *Energy Environ. Sci.* 10 (2017) 2563–2569.
- [35] Y. Ning, D. Ma, Y. Shen, F. Wang, X. Zhang, Constructing hierarchical mushroom-like bifunctional $\text{NiCo}/\text{NiCo}_2\text{S}_4/\text{NiCo}/\text{Ni}$ foam electrocatalysts for efficient overall water splitting in alkaline media, *Electrochim. Acta* 265 (2018) 19–31.
- [36] X. Li, C. Liu, Z. Fang, L. Xu, C. Lu, W. Hou, Ultrafast Room-temperature synthesis of self-supported NiFe -layered double hydroxide as large-current-density oxygen evolution electrocatalyst, *Small* 8 (2022), 2104354.
- [37] H.M. Sun, Z.H. Yan, F.M. Liu, W.C. Xu, F.Y. Cheng, J. Chen, Self-supported transition-metal-based electrocatalysts for hydrogen and oxygen evolution, *Adv. Mater.* 32 (2020) 18.
- [38] Q. Ji, Y. Kong, H. Tan, H. Duan, N. Li, B. Tang, Y. Wang, S. Feng, L. Lv, C. Wang, F. Hu, W. Zhang, L. Cai, W. Yan, Operando identification of active species and intermediates on sulfide interfaced by Fe_3O_4 for ultrastable alkaline oxygen evolution at large current density, *ACS Catal.* 12 (2022) 4318–4326.
- [39] H. Jiang, M. Sun, S. Wu, B. Huang, C.S. Lee, W. Zhang, Oxygen-incorporated NiMoP nanotube arrays as efficient bifunctional electrocatalysts for urea-assisted energy-saving hydrogen production in alkaline electrolyte, *Adv. Funct. Mater.* 31 (2021), 2104951.
- [40] H. Sun, Z. Yan, F. Liu, W. Xu, F. Cheng, J. Chen, Self-Supported transition-metal-based electrocatalysts for hydrogen and oxygen evolution, *Adv. Mater.* 32 (2020), 1806326.
- [41] J. Huang, H. Sheng, R.D. Ross, J. Han, X. Wang, B. Song, S. Jin, Modifying redox properties and local bonding of Co_3O_4 by CeO_2 enhances oxygen evolution catalysis in acid, *Nat. Commun.* 12 (2021) 3036.
- [42] Y. Liu, H. Zhang, H. Wan, W. Zhang, N. Jiang, G. Huang, Z. Wang, S. Luo, H. Sun, Tuning lithium storage properties of cubic Co_3O_4 crystallites: the effect of oxygen vacancies, *J. Alloy. Compd.* 787 (2019) 720–727.
- [43] S. Tan, Z. Xue, K. Tao, L. Han, Boosting energy storage performance of MOF-derived Co_3S_4 arrays via sulfur vacancy and surface engineering, *Chem. Commun.* 58 (2022) 6243–6246.
- [44] X. Li, K. Zheng, J. Zhang, G. Li, C. Xu, Engineering sulfur vacancies in spinel-phase Co_3S_4 for effective electrocatalysis of the oxygen evolution reaction, *ACS Omega* 7 (2022) 12430–12441.
- [45] H. Zhang, J. Zhang, Y. Li, H. Jiang, H. Jiang, C. Li, Continuous oxygen vacancy engineering of the Co_3O_4 layer for an enhanced alkaline electrocatalytic hydrogen evolution reaction, *J. Mater. Chem. A* 7 (2019) 13506–13510.
- [46] C. Zhang, Y. Shi, Y. Yu, Y. Du, B. Zhang, Engineering sulfur defects, atomic thickness, and porous structures into cobalt sulfide nanosheets for efficient electrocatalytic alkaline hydrogen evolution, *ACS Catal.* 8 (2018) 8077–8083.
- [47] Q. Zhang, P. Yang, H. Zhang, J. Zhao, H. Shi, Y. Huang, H. Yang, Oxygen vacancies in Co_3O_4 promote CO_2 photoreduction, *Appl. Catal. B* 300 (2022), 120729.
- [48] J. Liu, L. Zhang, H. Wu, D. Zang, Boosted electromagnetic wave absorption performance from vacancies, defects and interfaces engineering in $\text{Co(OH)F}/\text{Zn}_{0.76}\text{Co}_{0.24}\text{S}/\text{Co}_3\text{S}_4$ composite, *Chem. Eng. J.* 411 (2021), 128601.
- [49] J. Ji, K. Deng, J. Li, Z. Zhang, X. Duan, H. Huang, In situ transformation of 3D Co_3O_4 nanoparticles to 2D nanosheets with rich surface oxygen vacancies to boost hydrogen generation from NaBH_4 , *Chem. Eng. J.* 424 (2021), 130350.
- [50] S. Huang, Z. Jin, P. Ning, C. Gao, Y. Wu, X. Liu, P. Xin, Z. Chen, Y. Jiang, Z. Hu, Z. Chen, Synergistically modulating electronic structure of NiS_2 hierarchical architectures by phosphorus doping and sulfur-vacancies defect engineering enables efficient electrocatalytic water splitting, *Chem. Eng. J.* 420 (2021), 127630.
- [51] H. Chen, M. Yang, S. Tao, G. Chen, Oxygen vacancy enhanced catalytic activity of reduced Co_3O_4 towards p-nitrophenol reduction, *Appl. Catal. B* 209 (2017) 648–656.
- [52] X. Zhu, J. Dai, L. Li, D. Zhao, Z. Wu, Z. Tang, L.-J. Ma, S. Chen, Hierarchical carbon microflowers supported defect-rich Co_3S_4 nanoparticles: an efficient electrocatalyst for water splitting, *Carbon* 160 (2020) 133–144.
- [53] Q. Wang, X. Xue, Y. Lei, Y. Wang, Y. Feng, X. Xiong, D. Wang, Y. Li, Engineering of electronic states on Co_3O_4 ultrathin nanosheets by cation substitution and anion vacancies for oxygen evolution reaction, *Small* 16 (2020), 2001571.
- [54] Y. Liu, Y. Wen, Y. Zhang, X. Wu, H. Li, H. Chen, J. Huang, G. Liu, S. Peng, Reduced CoNi_2S_4 nanosheets decorated by sulfur vacancies with enhanced electrochemical performance for asymmetric supercapacitors, *Sci. China Mater.* 63 (2020) 1216–1226.
- [55] G. Zhou, G. Liu, X. Liu, Q. Yu, H. Mao, Z. Xiao, L. Wang, 1D/3D heterogeneous assembling body as trifunctional electrocatalysts enabling zinc-air battery and self-powered overall water splitting, *Adv. Funct. Mater.* 32 (2021), 2107608.
- [56] S. Du, Z. Ren, X. Wang, J. Wu, H. Meng, H. Fu, Controlled atmosphere corrosion engineering toward inhomogeneous NiFe-LDH for energetic oxygen evolution, *ACS Nano* 16 (2022) 7794–7803.
- [57] Y. Liu, Y. Bai, W. Yang, J. Ma, K. Sun, Self-supported electrode of $\text{NiCo-LDH}/\text{NiCo}_2\text{S}_4/\text{CC}$ with enhanced performance for oxygen evolution reaction and hydrogen evolution reaction, *Electrochim. Acta* 367 (2021), 137534.
- [58] Y. Zou, Y. Gu, B. Hui, X. Yang, H. Liu, S. Chen, R. Cai, J. Sun, X. Zhang, D. Yang, Nitrogen and sulfur vacancies in carbon shell to tune charge distribution of $\text{Co}_6\text{Ni}_3\text{S}_8$ Core and boost sodium storage, *Adv. Energy Mater.* 10 (2020), 1904147.